



# Massive $\text{Ti}^{3+}$ self-doped by the injected electrons from external Pt and the efficient photocatalytic hydrogen production under visible-Light

Yurong Yang<sup>a,c</sup>, Peng Gao<sup>a,b,\*</sup>, Xiaochen Ren<sup>a</sup>, Linna Sha<sup>a</sup>, Piaoping Yang<sup>a, \*\*</sup>, Jianjiao Zhang<sup>a</sup>, Yujin Chen<sup>a, \*\*</sup>, Lei Yang<sup>d, \*\*</sup>

<sup>a</sup> Key Laboratory of Superlight Materials and Surface Technology, Ministry of Education, College of Materials Science and Chemical Engineering, Harbin Engineering University, Harbin, Heilongjiang, 150001, PR China

<sup>b</sup> College of Materials Science and Chemical Engineering, Hangzhou Normal University, Hangzhou, Zhejiang, 310026, PR China

<sup>c</sup> College of Science, Heihe University, Heihe, Heilongjiang, 164300, PR China

<sup>d</sup> Center of Analysis Measurement, Harbin Institute of Technology, Harbin, Heilongjiang, 150001, PR China



## ARTICLE INFO

### Article history:

Received 25 May 2017

Received in revised form 22 June 2017

Accepted 6 July 2017

Available online 8 July 2017

### Keywords:

$\text{Ti}^{3+}$  self-doped

Pt-C

Photocatalytic hydrogen production

Visible-light

## ABSTRACT

$\text{Ti}^{3+}$  doping in  $\text{TiO}_2$  photocatalyst has attracted much attention due to its enhanced visible-light absorption and the decreased carrier recombination. However, the introduction of massive stable  $\text{Ti}^{3+}$  is still a great challenge because  $\text{Ti}^{3+}$  is easy to be oxidized in air. In this work, for the first time, a negatively charged core/shell  $\text{TiO}_2/\text{C}$  nanostructure is prepared and then  $\text{Pt}^0$  atoms reduced by  $\text{NaBH}_4$  are loaded on its surface. Through a tracking test of the product's Zeta potential, XPS and FTIR measurements, it is found that the reductive electrons are produced due to the reaction between C and metal Pt, in which Pt exhibits a +2 chemical valence. And the lost electrons by Pt are transferred into the interior  $\text{TiO}_2$  through the carbon shell and reduce  $\text{Ti}^{4+}$  to  $\text{Ti}^{3+}$ . This method avoids  $\text{Ti}^{3+}$  ions' exposing to air and overcomes the complex coating process for isolating oxygen, and provides a new facile one for efficiently  $\text{Ti}^{3+}$  self-doping. Through the following measurements, such as XPS, PL, EPR and Raman etc., it is proved that massive  $\text{Ti}^{3+}$  ions are formed in the interior  $\text{TiO}_2$ , which greatly narrows the composite's band-gap (from 3.11 eV to 2.47 eV) and enhances the visible-light absorption. As a result, the as-obtained sample exhibits a larger carrier densities ( $13.9 \times 10^{18} \text{ cm}^{-3}$ ) and a higher photocatalytic activity under visible-light irradiation compared with those in other literatures: the rate of photocatalytic water splitting for  $\text{H}_2$  generation is up to  $8117 \mu\text{mol h}^{-1} \text{ g}^{-1}$ .

© 2017 Elsevier B.V. All rights reserved.

## 1. Introduction

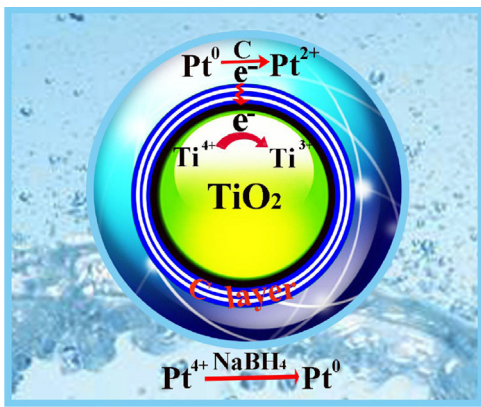
$\text{Ti}^{3+}$  doping has been extensively studied in the  $\text{TiO}_2$  based materials for photocatalytic hydrogen generation, solar cells, waste water purification, and solar thermal collectors etc. [1–5]. The doping brings several outstanding benefits, such as narrowing the band gap [1], enhancing effective visible-light absorption [3] and reducing carrier recombination centers [4]. However, it is also found that the low quantity of  $\text{Ti}^{3+}$  in  $\text{TiO}_2$  leads to the production of localized oxygen vacancy states under the conduction band minimum of  $\text{TiO}_2$ , which damages the flow of electrons and thus lowers the

photocatalytic activity [6,7]. Conversely, the high concentration of  $\text{Ti}^{3+}$  in  $\text{TiO}_2$  promotes the flow of electrons and enhances the photocatalytic activity [8–10]. It is also noted that  $\text{Ti}^{3+}$  is extremely unstable in the air and can be rapidly oxidized, which often results in a small quantity of  $\text{Ti}^{3+}$  self-doping in many previous works [11–14]. So the realization of an abundant and stable  $\text{Ti}^{3+}$  doping in  $\text{TiO}_2$  through a facile method is still a big challenge. So far, a series of studies have been attempted to dope a large number of stable  $\text{Ti}^{3+}$  in  $\text{TiO}_2$  by some man-made strategies, such as hydrogenation [15,16], high energy particle bombardment (laser, electron or  $\text{Ar}^+$ ) [17–19], redox with reducing agents (Zn, Al, DEG,  $\text{NaBH}_4$ , CO) [12,20–23], photochemical synthesis [24,25], and partial oxidation of Ti based low valent compounds ( $\text{TiH}_2$ ,  $\text{TiO}$ ,  $\text{Ti}_2\text{O}_3$  and  $\text{TiCl}_3$ ) [26–28]. However, all the above strategies have their own shortages, such as complex experimental process, high-price cost, expensive agents, especially low doping quantity and weak stability. These problems promote many researchers to explore a new method for efficiently  $\text{Ti}^{3+}$  self-doping.

\* Corresponding author at: Key Laboratory of Superlight Materials and Surface Technology, Ministry of Education, College of Materials Science and Chemical Engineering, Harbin Engineering University, Harbin, Heilongjiang, 150001, PR China.

\*\* Corresponding authors.

E-mail addresses: [gaopeng@hrbeu.edu.cn](mailto:gaopeng@hrbeu.edu.cn) (P. Gao), [yangpiaoping@hrbeu.edu.cn](mailto:yangpiaoping@hrbeu.edu.cn) (P. Yang), [chenyujin@hrbeu.edu.cn](mailto:chenyujin@hrbeu.edu.cn) (Y. Chen), [yanglei8399@163.com](mailto:yanglei8399@163.com) (L. Yang).



**Scheme 1.** The formation mechanism of  $\text{Ti}^{3+}$  in  $\text{TiO}_2$ .

In this work, as shown in **Scheme 1**, it is found by us that the reductive electrons are produced due to the formation of a Pt-C bond between C in the negatively charged  $\text{TiO}_2/\text{C}$  sample and metal Pt, in which Pt exhibits a +2 chemical valence. Then the electrons are easily transferred into the interior  $\text{TiO}_2$  through the outside carbon shell then reduce  $\text{Ti}^{4+}$  to  $\text{Ti}^{3+}$ , in which the as-coated carbon is used as a shield for protecting  $\text{Ti}^{3+}$  from oxidation. The measurement results prove that a large number of stable  $\text{Ti}^{3+}$  are formed in the carbon-coated  $\text{TiO}_2$  after this simple chemical treatment. And the as-obtained sample exhibits a high catalytic activity (up to  $8117 \mu\text{mol h}^{-1} \text{g}^{-1}$ ) for hydrogen generation through water splitting under visible-light and a large carrier densities ( $13.9 \times 10^{18} \text{ cm}^{-3}$ ). This rate of photocatalytic for  $\text{H}_2$  generation is around 16 times of that of the sample without  $\text{Ti}^{3+}$  doping ( $507 \mu\text{mol h}^{-1} \text{g}^{-1}$ ).

## 2. Experimental section

### 2.1. Preparation of $\text{TiO}_2$ nanorods

All the chemicals were of analytical grade.  $\text{TiO}_2$  nanorods were synthesized according to the literature [29] using an alkaline hydrothermal process.

### 2.2. Preparation of $\text{TiO}_2/\text{C}$ NTS

$\text{TiO}_2/\text{C}$  nanorods were prepared by a vacuum infiltration process. In a typical procedure, 0.1 g glucose was first stirred in deionized water (40 mL) under high purity nitrogen gas for 1 h. Then 1 g  $\text{TiO}_2$  nanorods were added into the above solution under argon atmosphere and stirred for 4 h. Finally, the resulting sample was carbonized at  $400^\circ\text{C}$  for 2 h under argon atmosphere with a heating rate of  $10^\circ\text{C min}^{-1}$ .

### 2.3. Preparation of $\text{Ti}^{3+}$ doped $\text{TiO}_2/\text{C}$ nanorods

$\text{Ti}^{3+}$  doped  $\text{TiO}_2/\text{C}$  nanorods have been synthesized by a simple chemical reduction method, which were named as  $\text{Ti}^{3+}/\text{TCP}$ . In a typical procedure,  $\text{TiO}_2/\text{C}$  nanorods (1 g) were dispersed in a  $\text{H}_2\text{PtCl}_6$  aqueous solution (0.005 M, 40 mL), and vigorously agitated for 2 h. Then 0.1 M  $\text{NaBH}_4$  cold aqueous solution was dropwise added in it and stirred for 4 h. The molar ratio of Pt to  $\text{NaBH}_4$  is 1:10. Finally, the resultant sample was collected by centrifuged and washed with distilled water and ethanol, dried in a vacuum furnace at  $60^\circ\text{C}$  for 24 h.  $\text{TiO}_2/\text{Pt}$  sample was prepared by the same chemical reduction method, in which  $\text{TiO}_2$  was used as precursor. And  $\text{Ti}^{3+}/\text{TCP}$ -F was prepared through a similar procedure, only adding few  $\text{H}_2\text{PtCl}_6$  aqueous solution (0.005 M, 25 mL).

### 2.4. Preparation of $\text{TiO}_2/\text{C}/\text{Pt}$ nanorods

$\text{TiO}_2/\text{C}/\text{Pt}$  nanorods were prepared by a mechanical mixing of  $\text{TiO}_2/\text{C}$  nanorods with Pt nanoparticles (0.2 mM) reduced by the similar reduction method.

## 3. Results and discussions

### 3.1. Structures and compositions

The chemical composition and valence state of the elements in the  $\text{Ti}^{3+}/\text{TCP}$  composite are firstly analyzed by X-ray photoelectron spectroscopy (XPS) measurements. Fig. 1a show the Ti 2p of the  $\text{Ti}^{3+}/\text{TCP}$  sample. Compared to the Ti 2p XPS spectra (Fig. S3a) of the  $\text{TiO}_2/\text{C}$  sample, there are two additional peaks at 457.6 ( $\text{Ti} 2p_{3/2}$ ) and 463.2 eV ( $\text{Ti} 2p_{1/2}$ ), which are typical characteristic peaks of the  $\text{Ti}^{3+}$ .<sup>12</sup> In addition, the other two peaks centered at 458.7 and 464.5 eV, which are consistent with  $\text{Ti}^{4+}$  in  $\text{TiO}_2$  lattice [30]. The quantitative analysis of XPS results illustrates that abundant  $\text{Ti}^{3+}$  and  $\text{Ti}^{4+}$  are coexisted in the  $\text{Ti}^{3+}/\text{TCP}$  sample. Fig. 1b show the O 1s spectra of the  $\text{Ti}^{3+}/\text{TCP}$  sample. Obviously, it can be seen that there are two peaks, the peak at 529.2 eV is assigned to  $\text{Ti}^{4+}-\text{O}$ , and the other peak at 530.2 eV is assigned to  $\text{Ti}^{3+}-\text{O}$  or  $-\text{OH}$  in the  $\text{Ti}^{3+}/\text{TCP}$  sample [8,14]. Fig. 1c shows the C 1s XPS spectra of the  $\text{Ti}^{3+}/\text{TCP}$  sample. The peak around 284.6 and 288.6 eV are attributed to  $\text{C}=\text{C}$  bond and  $\text{C}=\text{O}$  bond, respectively [31,32]. Interestingly, after  $\text{NaBH}_4$  reducing, not all the Pt atoms are  $\text{Pt}^{4+}$  and  $\text{Pt}^0$ . As shown in Fig. 1d, the  $4f_{7/2}$  and  $4f_{5/2}$  characteristic peaks of  $\text{Pt}^0$  are observed at 71.3 and 74.9 eV [33], respectively. And the peaks attributed to the  $4f_{7/2}$  and  $4f_{5/2}$  of  $\text{Pt}^{2+}$  are also found at 72.2 and 75.8 eV [33], respectively. Furthermore, the two peaks at 74.2 and 77.3 eV are derived from the  $4f_{7/2}$  and  $4f_{5/2}$  of  $\text{Pt}^{4+}$  [33].

X-ray diffraction (XRD) analysis is further conducted to characterize the compositions of raw  $\text{TiO}_2$  and  $\text{TiO}_2/\text{C}$ ,  $\text{Ti}^{3+}/\text{TCP}$  sample. As shown in Fig. 2a, peaks appeared in the  $\text{TiO}_2$ ,  $\text{TiO}_2/\text{C}$ ,  $\text{Ti}^{3+}/\text{TCP}$  nanorods can be well indexed to an anatase phased  $\text{TiO}_2$  (JCPDS No. 21-1272). No diffraction peak of C are observed because of its little amount. And no obvious shift of the  $\text{TiO}_2$  diffraction peaks and lattice deformation are found. In order to further demonstrate the presence of  $\text{Ti}^{3+}$ , electron para-magnetic resonance (EPR) and vibrating sample magnetometer (VSM) measurements are employed. As shown in Fig. 2b, a sharp and steep signal at  $g=1.98$  certainly indicates the massive existence of  $\text{Ti}^{3+}$  in the  $\text{Ti}^{3+}/\text{TCP}$  sample [34]. EPR has also been carried out to detect the presence of  $\text{Ti}^{3+}$  in  $\text{TiO}_2$  and  $\text{TiO}_2/\text{C}$  samples. As shown in Fig. S5, the EPR characteristic peak of  $\text{Ti}^{3+}$  isn't found, which further confirms the absence of  $\text{Ti}^{3+}$  in  $\text{TiO}_2$  and  $\text{TiO}_2/\text{C}$  samples. In addition, the standard hysteresis loop of the  $\text{Ti}^{3+}/\text{TCP}$  sample (Fig. S6) also clearly evidences the presence of  $\text{Ti}^{3+}$ . The  $\text{Ti}^{3+}/\text{TCP}$  nanorods show a relatively stronger saturation magnetizations ( $M_s$ ) of 0.02 emu/g compared to  $\text{Ti}^{3+}$  doped  $\text{TiO}_2$  samples reduced by Al in the literature [1], which means that a large number of stable  $\text{Ti}^{3+}$  doping in  $\text{TiO}_2$ . Raman spectroscopy is also conducted to affirm the atoms' status, as illustrated in Fig. 2c and Fig. S7. The spectra of  $\text{TiO}_2/\text{C}$  and  $\text{Ti}^{3+}/\text{TCP}$  exhibit four same peaks at  $143 \text{ cm}^{-1}$ ,  $394 \text{ cm}^{-1}$ ,  $512 \text{ cm}^{-1}$  and  $633 \text{ cm}^{-1}$  respectively, attributed to the anatase  $\text{TiO}_2$  [35]. In addition, the peak located at about  $1360 \text{ cm}^{-1}$  is the D peak of carbon, denoting to the edge distortion and structural disorder of carbon [30]. And the other peak at about  $1590 \text{ cm}^{-1}$  is the G peak of carbon associated with the graphitic carbon [30]. The G/D intensity ratio of  $\text{Ti}^{3+}/\text{TCP}$  is 2.63, which is smaller than that of  $\text{TiO}_2/\text{C}$  (2.83), indicating that an increased disorder of the graphene structures after Pt loading. Meanwhile, compared with the Raman spectrum of  $\text{TiO}_2/\text{C}$ , the D and G peaks of the  $\text{Ti}^{3+}/\text{TCP}$  sample show an obvious blue shift, indicating that a strong interaction between  $\text{TiO}_2$

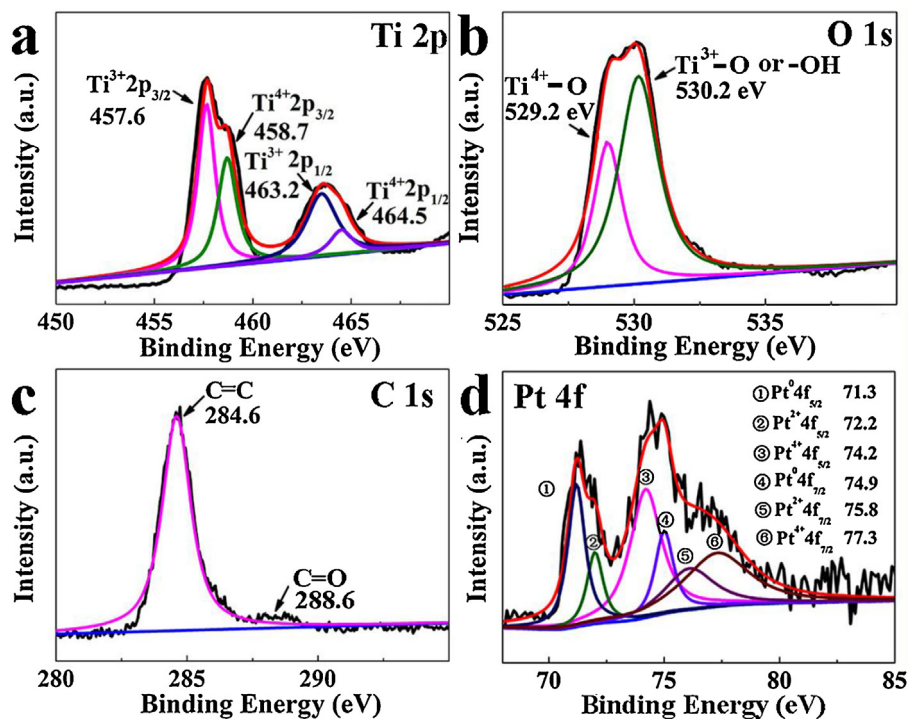


Fig. 1. XPS of  $\text{Ti}^{3+}$ /TCP sample. (a) Ti 2p spectra; (b) O 1s spectra; (c) C 1s spectra; (d) Pt 4f spectra.

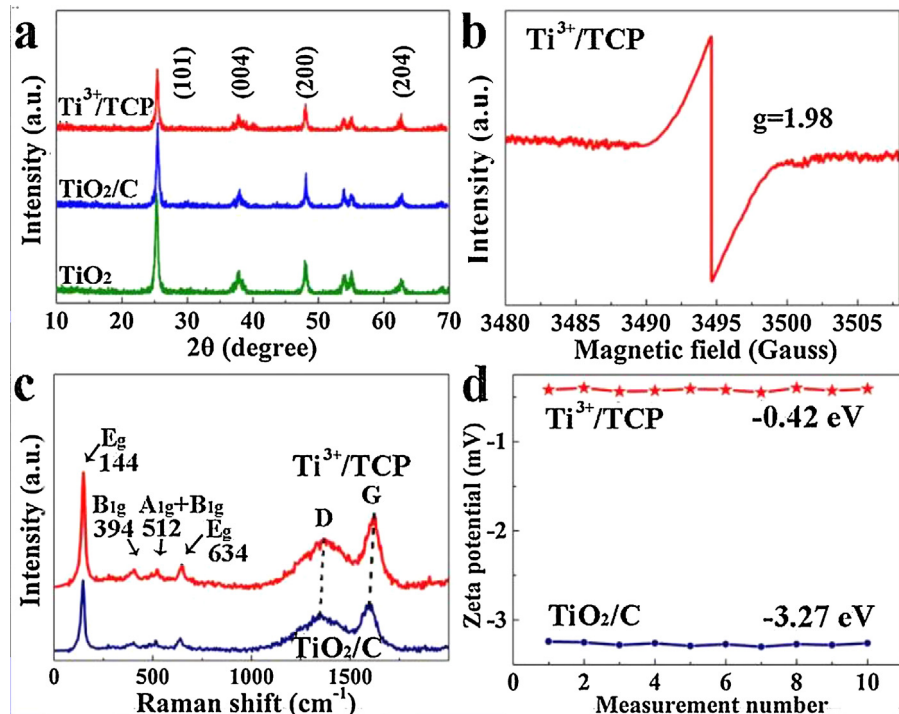
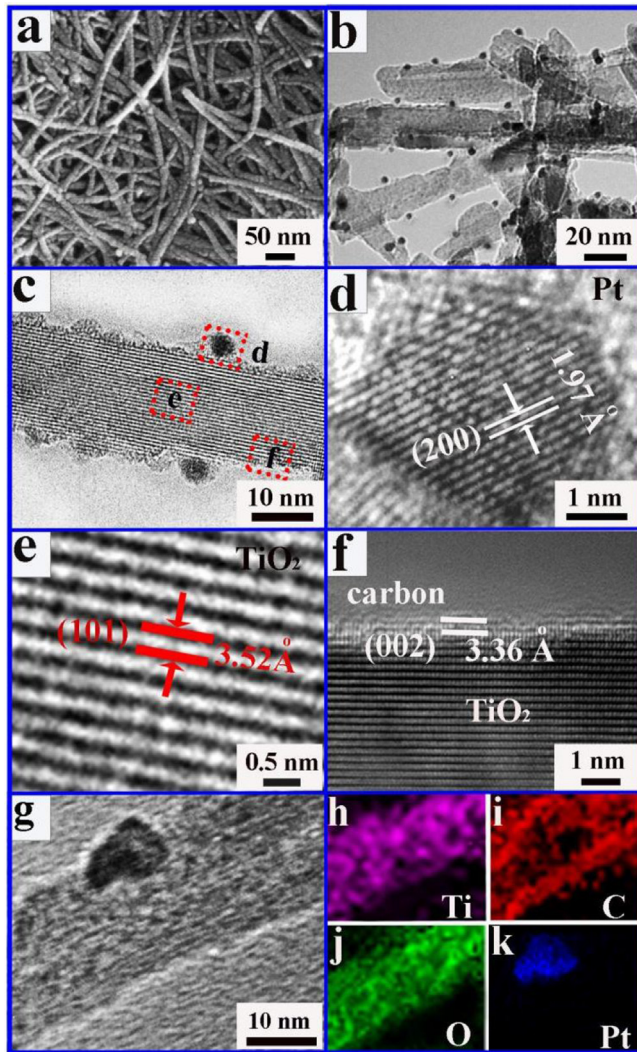


Fig. 2. (a) XRD patterns of the  $\text{TiO}_2$ ,  $\text{TiO}_2/\text{C}$  and  $\text{Ti}^{3+}/\text{TCP}$  samples. (b) EPR spectra of the  $\text{Ti}^{3+}/\text{TCP}$  sample. (c) Raman spectra of the  $\text{TiO}_2/\text{C}$  and  $\text{Ti}^{3+}/\text{TCP}$  samples. (d) Zeta potential of the  $\text{TiO}_2/\text{C}$  and  $\text{Ti}^{3+}/\text{TCP}$  samples.

and the carbon sheets after Pt loading. Zeta potentials of  $\text{TiO}_2/\text{C}$  and  $\text{Ti}^{3+}/\text{TCP}$  nanorods are shown in Figs. 2 d and S8. The Zeta potential of the raw  $\text{TiO}_2/\text{C}$  nanorods is  $-3.27 \text{ eV}$ . However, after  $\text{Ti}^{3+}$  doping and Pt loading, the Zeta potential increased to  $-0.42 \text{ eV}$ . The greatly increased potential are mainly due to the presence of abundant  $\text{Pt}^{2+}$  and  $\text{Pt}^{4+}$  ions existed on the surface of the  $\text{Ti}^{3+}/\text{TCP}$  sample.

Figs. 3 a and S9 shows the scanning electron microscopy (SEM) images of the  $\text{Ti}^{3+}/\text{TCP}$ ,  $\text{TiO}_2$  and  $\text{TiO}_2/\text{C}$  samples. Clearly, it can

be seen that the raw  $\text{TiO}_2$  nanorods with rather smooth surfaces are around  $17 \text{ nm}$  in diameter and  $400 \text{ nm}$  in length. After carbon-coating and Pt loading respectively, the diameter of  $\text{TiO}_2$  nanorods varies from  $15 \text{ nm}$  to  $20 \text{ nm}$ . The morphology and structure of the  $\text{Ti}^{3+}/\text{TCP}$  sample are further characterized by transmission electron microscopy (TEM) and high-resolution transmission electron microscopy (HRTEM). As shown in Fig. 3b of its TEM images, it is clear to see that about  $4 \text{ nm}$  Pt nanoparticles are well dispersed on



**Fig. 3.** SEM, TEM and HRTEM images of the  $\text{Ti}^{3+}$ /TCP sample. (a) and (b) SEM and TEM images of the  $\text{Ti}^{3+}$ /TCP nanorods; (c) HRTEM images of a typical nanorod; (d), (e) and (f) The enlarged HRTEM image of Pt section,  $\text{TiO}_2$  section and the interface section; (g)–(k) TEM image of a typical  $\text{Ti}^{3+}$ /TCP nanorod and its corresponding EDS element mappings of Ti, O, C and Pt elements.

every nanorod's surface, which roughen the nanorods and increase the sample's effective surface area. The following corresponding  $\text{N}_2$  adsorption-desorption isotherm measurement results confirm the above presumption. As shown in Fig. S10, the surface areas of  $\text{Ti}^{3+}$ /TCP and  $\text{TiO}_2/\text{C}$  samples are  $159.01 \text{ m}^2 \text{ g}^{-1}$  and  $149.22 \text{ m}^2 \text{ g}^{-1}$  respectively, which are greatly higher than that of  $\text{TiO}_2$  precursor ( $117.86 \text{ m}^2 \text{ g}^{-1}$ ). The HRTEM images of the framed areas in Fig. 3c–f show the lattice fringe spacings of 3.52, 3.36 and 1.97 Å, corresponding to the (101) plane of  $\text{TiO}_2$ , (002) plane of graphitic carbon and (200) plane of Pt, respectively. In addition, the thickness of the carbon sheets is about 1.08 nm and consists of three carbon atom-layers, as shown in Fig. 3f. The TEM images and EDS mappings (Fig. 3g–k) also verify the composition of the sample:  $\text{TiO}_2$  as a core, carbon sheet as a shell and Pt dispersed on the surface.

### 3.2. The conversion mechanism from $\text{Ti}^{4+}$ to $\text{Ti}^{3+}$

As listed in the following equations of the oxidation-reduction potentials among  $\text{Pt}^0$ ,  $\text{Pt}^{2+}$  and  $\text{Pt}^{4+}$ ,



When  $\text{Pt}^{4+}$  is treated with a reductive agent, it will be transformed into  $\text{Pt}^0$  quickly, which has been confirmed in many literatures [36–39]. So in this our work, for the first time,  $\text{Pt}^{4+}$  added in the system is reduced to  $\text{Pt}^0$  by  $\text{NaBH}_4$ , which is proved by a XPS measurement of the sample obtained by condensing the reaction solution. As shown in Fig. S11, only  $\text{Pt}^0$  and  $\text{Pt}^{4+}$  are found in the sample, without  $\text{Pt}^{2+}$ . This means that  $\text{Pt}^{2+}$  subsequently appears after  $\text{Pt}^0$  forming in the solution and landing on  $\text{TiO}_2/\text{C}$ . The formation of  $\text{Pt}^{2+}$  should be due to the reaction (Eq. (4)) between the negatively charged carbon (as indicated in Fig. 2d of the Zeta potential of  $\text{TiO}_2/\text{C}$ ) and  $\text{Pt}^0$ , which has also been found in recent works [33,40].



In this process, Pt–C chemical bonds are constructed. Their Raman results in Fig. 2c also testifies the changes induced by Pt–C bonds. As shown in Fig. 2c, the blue shifts of D and G peaks of carbon demonstrate that the stress induced by Pt–C bonds between Pt and carbon layers [41]. In order to further demonstrates the formation of Pt–C bonds, Fourier transform infrared (FTIR) measurements were conducted. As shown in Fig. S12, the peak at  $458 \text{ cm}^{-1}$  corresponds to the stretching vibration of O–Ti–O [42]. The C=C stretching vibration of the coated carbon layer at  $1630 \text{ cm}^{-1}$  is also found [43]. The signal at  $3400 \text{ cm}^{-1}$  is the characteristic peak of the surface –OH groups [44]. Notably, the peak appeared at  $1092 \text{ cm}^{-1}$  is assigned to the stretching vibration of Pt–C [45]. In addition, two peaks centered at  $1469 \text{ cm}^{-1}$  and  $3030 \text{ cm}^{-1}$  represent the C–H stretching vibration [46]. Obviously, a blue shift of the C–H stretching vibration peaks in the  $\text{Ti}^{3+}$ /TCP sample is observed compared with that of  $\text{TiO}_2/\text{C}/\text{Pt}$ , which further proves the formation of Pt–C bonds [47]. Moreover, TG measurements in an air atmosphere further indicate the formation of Pt–C bonds. Fig. S13 shows the TG curves of  $\text{TiO}_2/\text{C}/\text{Pt}$  and  $\text{Ti}^{3+}$ /TCP. Clearly, a same weight loss (2.5%) is found in two samples due to the combustion of carbon. However, the combustion temperature region of carbon in  $\text{Ti}^{3+}$ /TCP (25–513 °C) is longer than that of  $\text{TiO}_2/\text{C}/\text{Pt}$  (25–424 °C), indicating a higher thermal stability of  $\text{Ti}^{3+}$ /TCP. This can be ascribed to that the carbon layer is stabilized by the Pt nanoparticles due to the strong chemical coupling with the formation of Pt–C.

The redundant electrons lost by  $\text{Pt}^0$  are transferred into the interior  $\text{TiO}_2$  through the carbon layer and reduce  $\text{Ti}^{4+}$  to  $\text{Ti}^{3+}$ , as shown in Scheme 1 and the following equation:



In order to confirm that the reduction of  $\text{Ti}^{4+}$  in  $\text{TiO}_2$  is induced by Pt,  $\text{TiO}_2/\text{C}$  sample is treated with a similar chemical reduction procedure, only without  $\text{H}_2\text{PtCl}_6$ . As shown in Fig. S3c, no characteristic peak of the  $\text{Ti}^{3+}$  is detected. However, after adding a little  $\text{H}_2\text{PtCl}_6$  aqueous solution (0.005 M, 25 mL), it is clear to see that the characteristic XPS peaks of  $\text{Ti}^{3+}$  are exhibited (Fig. 4a). The differences convincingly prove that the reduction of  $\text{Ti}^{4+}$  in  $\text{TiO}_2$  is induced by  $\text{Pt}^0$ . Notably, it is clearly observed that the content of  $\text{Ti}^{3+}$  in this sample (Fig. 4a) is less than that of  $\text{Ti}^{3+}$ /TCP (Fig. 1a). It means that with the Pt content increasing, the  $\text{Ti}^{3+}$  content are obviously increased, which further confirms that the direct relation between the reduction of  $\text{Ti}^{4+}$  in  $\text{TiO}_2$  and Pt addition.

### 3.3. Photocatalytic hydrogen production performance

Photocatalytic hydrogen production performance In this work, photoluminescence (PL) measurements is firstly used to evaluate the behavior of charges' separation and transport in the photocatalysts. As shown in Fig. 5a, the PL spectrum of  $\text{Ti}^{3+}$ /TCP exhibits

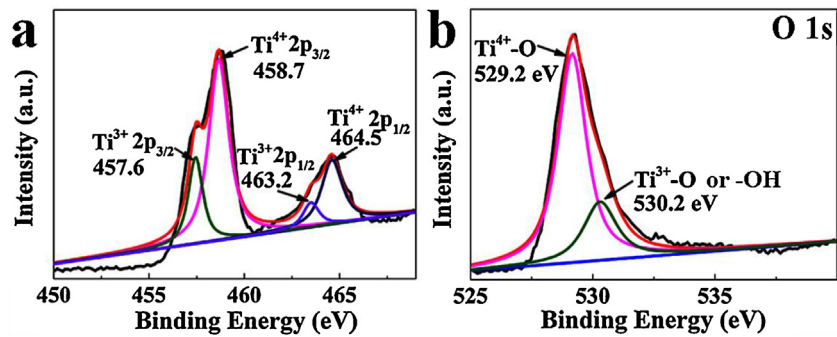


Fig. 4. The Ti 2p (a) and O 1s (b) XPS spectra of the  $\text{Ti}^{3+}$ /TCP sample with a less addition of  $\text{H}_2\text{PtCl}_6$  (0.005 M, 25 mL).

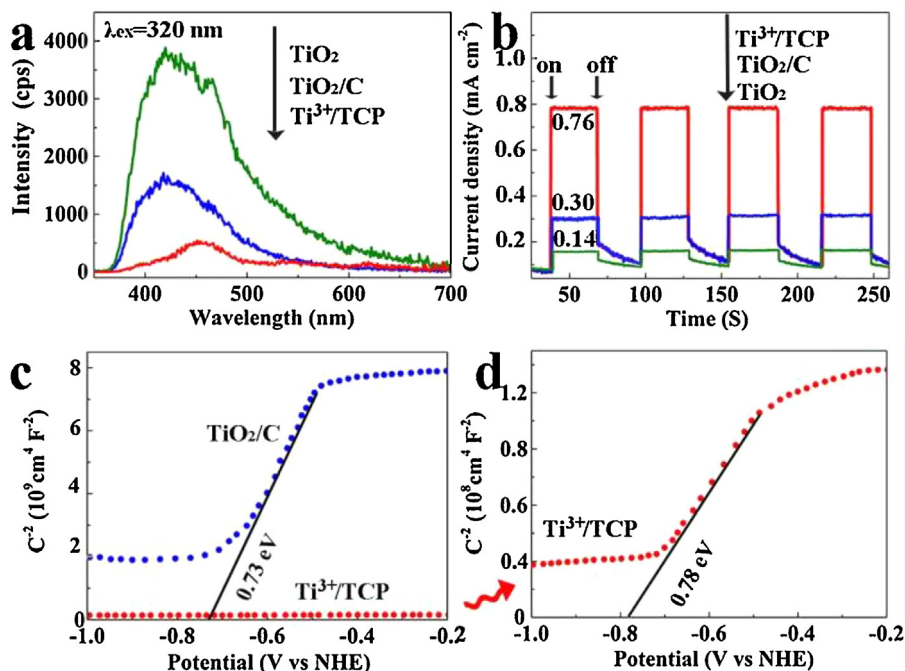


Fig. 5. (a) PL spectra of the  $\text{TiO}_2$ ,  $\text{TiO}_2/\text{C}$  and  $\text{Ti}^{3+}/\text{TCP}$  samples; (b) Photocurrent densities of the  $\text{TiO}_2$ ,  $\text{TiO}_2/\text{C}$  and  $\text{Ti}^{3+}/\text{TCP}$  samples; (c) and (d) Mott-Schottky plots of the  $\text{TiO}_2/\text{C}$  and  $\text{Ti}^{3+}/\text{TCP}$  samples examined in the dark.

an extremely weak signal compared to those of  $\text{TiO}_2$  and  $\text{TiO}_2/\text{C}$ , implying a lower recombination efficiency of excited electrons and holes [48]. This demonstrates that such a stable and abundant  $\text{Ti}^{3+}$  doping realizes a highly efficient separation of electron-hole pairs. Furthermore, the transient photocurrent responses of the samples with a same amount are tested under intermittent visible-light irradiation to further verify the separation effect. As shown in Fig. 5b, the transient photocurrent density of the  $\text{Ti}^{3+}/\text{TCP}$  nanorods is  $0.76 \text{ mA cm}^{-2}$ , which is much higher than those of  $\text{TiO}_2$  and  $\text{TiO}_2/\text{C}$  nanorods ( $\text{TiO}_2$ :  $0.14 \text{ mA cm}^{-2}$ ,  $\text{TiO}_2/\text{C}$ :  $0.30 \text{ mA cm}^{-2}$ ). The remarkably improved photocurrent density indicates more electrons are produced and transferred in  $\text{Ti}^{3+}/\text{TCP}$  due to the introduction of  $\text{Ti}^{3+}$ , which agrees with the PL measurement analysis. To further demonstrate the quick separation transport behaviors of charges in the  $\text{Ti}^{3+}/\text{TCP}$  sample, electrochemical impedance spectra (EIS) is carried out in the dark and under visible-light irradiation, as shown in Fig. S16. Clearly, EIS spectrum of the sample both in the dark and under irradiation shows a semi-circle, indicating that it is charge transfer resistance limits the kinetics at the semiconductor interface [49–51]. Meanwhile, all the arc radii under irradiation are much smaller than those in the dark because of increased electron conductivity, which is well in accordance with those reported

in the previous literatures [52,53]. Notably, the  $\text{Ti}^{3+}/\text{TCP}$  sample shows the smallest arc radius in all samples upon visible-light irradiation, suggesting a considerably effective charge separation and transport induced by the introduction of stable abundant  $\text{Ti}^{3+}$ . In addition, we measured the sample's carrier density through a Mott-Schottky method. As shown in Fig. 5c and d, the Mott-Schottky plots of  $\text{TiO}_2/\text{C}$  and  $\text{Ti}^{3+}/\text{TCP}$  nanorods show a positive slope, indicating that in these n-type semiconductors their Fermi level are about  $-0.73 \text{ eV}$  and  $-0.78 \text{ eV}$  (vs NHE) for  $\text{TiO}_2/\text{C}$  and  $\text{Ti}^{3+}/\text{TCP}$ , respectively. Moreover, according to the slopes of Mott-Schottky plots, carrier densities are calculated using the following equation [53]:

$$N_d = \frac{2}{e_0 \varepsilon \varepsilon_0} / \frac{d(1/C^2)}{dV} \quad (6)$$

where  $e_0$  is the electronic charge,  $\varepsilon$  and  $\varepsilon_0$  the dielectric constant of  $\text{TiO}_2$  and the permittivity of vacuum, respectively,  $N_d$  is the carrier density,  $C$  is interfacial capacitance, and  $V$  is the applied voltage. In contrast, the carrier density of  $\text{Ti}^{3+}/\text{TCP}$  ( $13.9 \times 10^{18} \text{ cm}^{-3}$ ) is almost elevated to 10 times compared with that of  $\text{TiO}_2/\text{C}$  ( $1.42 \times 10^{18}$ ). It verifies that the introduction of abundant  $\text{Ti}^{3+}$  remarkably accelerates carrier's transfer, which well agrees with their photocurrent response results.

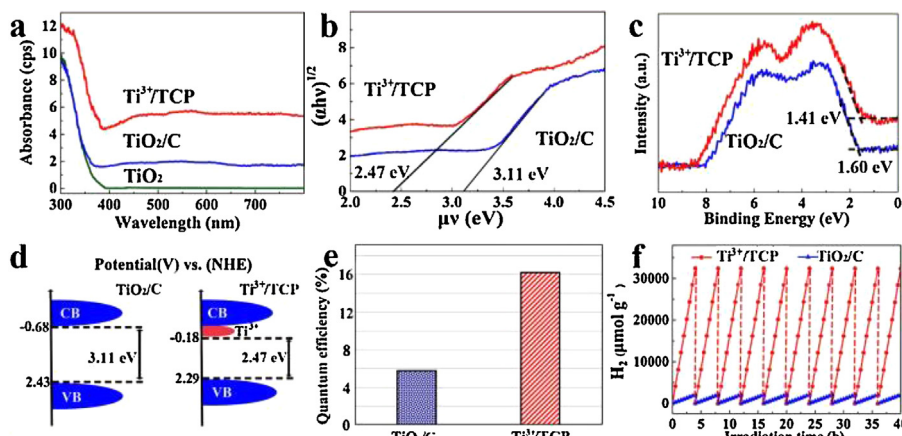


**Fig. 6.** (a) UV-vis DRS of the TiO<sub>2</sub>, TiO<sub>2</sub>/C and Ti<sup>3+</sup>/TCP samples. (b) Optical band gaps determined by the UV-vis DRS. (c) Valence-band spectra measured by XPS. (d) The band structures of the TiO<sub>2</sub>/C and Ti<sup>3+</sup>/TCP nanorods. (e) The quantum efficiency of TiO<sub>2</sub>/C and Ti<sup>3+</sup>/TCP nanorods. (f) Visible-light driven photocatalytic water splitting for H<sub>2</sub> generation in 10 repeated cycles (4 h/cycle).

Furthermore, the band gaps of the samples are analyzed by ultraviolet-visible diffuse reflectance spectrum (UV-vis DRS), as shown in Fig. 6a. Obviously, as shown in Fig. 6a, the visible-light absorption of TiO<sub>2</sub> nanorods is obviously enhanced after carbon coating. This is also proved by their color change from white to gray, as shown in Fig. S2. Notably, compared to that of TiO<sub>2</sub>/C, the visible-light absorption intensity of Ti<sup>3+</sup>/TCP is greatly increased because of the narrowed band gap induced by abundant Ti<sup>3+</sup> doping. Additionally, as a protective shield, carbon shell isolates the outside oxygen and strengthens the stability of Ti<sup>3+</sup>. In order to gain deeper insight into the change of energy band structures, according to the plots of the transformed Kubelka-Munk function of UV-vis DRS (Fig. 6b), the band gaps of TiO<sub>2</sub>/C, Ti<sup>3+</sup>/TCP are characterized as 3.11 eV and 2.47 eV, respectively. The energy band structures of TiO<sub>2</sub>/C and Ti<sup>3+</sup>/TCP are further ascertained by valence band (VB) XPS measurements, as shown in Fig. 6c. Apparently, the VB top of 1.60 and 1.41 eV below the Fermi level (E<sub>F</sub>) are seen for TiO<sub>2</sub>/C and Ti<sup>3+</sup>/TCP, respectively. The valence band values of TiO<sub>2</sub>/C and Ti<sup>3+</sup>/TCP are 2.43 eV and 2.29 eV versus normal hydrogen electrode after a calibration with reference Fermi level, respectively. Compared with TiO<sub>2</sub>/C, the valence band top of Ti<sup>3+</sup>/TCP shifts upward 0.14 eV and its conduction band shifts downward 0.50 eV, which originate from the introduction of abundant Ti<sup>3+</sup>. Based on the above results, the energy band structures of TiO<sub>2</sub>/C and Ti<sup>3+</sup>/TCP nanorods are depicted in Fig. 6d. As shown in Fig. 6e and f, the TiO<sub>2</sub>/C sample show good quantum efficiency (5.8%) and photocatalytic hydrogen production performance (507 μmol h<sup>-1</sup> g<sup>-1</sup>) under visible-light irradiation. Apart from the enhanced visible-light absorption, the improved photocatalytic performance is also attributed to the greatly enhanced electrical conductivity of TiO<sub>2</sub> induced by the carbon layers, leading to a rapid transportation and separation of photon-generated electrons and holes [54]. Most importantly, the Ti<sup>3+</sup>/TCP sample shows a significantly high H<sub>2</sub> evolution rate of 8117 μmol h<sup>-1</sup> g<sup>-1</sup> and an excellent quantum efficiency up to 16.2% at 420 nm, which is much higher than those of TiO<sub>2</sub>/C nanorods. Furthermore, the H<sub>2</sub> evolution rate is much higher than other similar composites reported in literatures (Table S1), though under a lower energy illustration in our work. Moreover, the Ti<sup>3+</sup>/TCP sample exhibits a good catalytic stability, which retains its high photocatalytic activity even after a 40 h cycle reaction.

#### 4. Conclusions

In summary, a large number of stable Ti<sup>3+</sup> doping in TiO<sub>2</sub> is realized through a facile Pt-induced chemical reduction method.

Through a serial of detailed measurements and analysis, it is demonstrated that Ti<sup>3+</sup>/TCP sample exhibits an enhanced visible-light absorption. Resultantly, its photocatalytic hydrogen generation under visible-light is greatly enhanced and maintains a good stability. This strategy open a new window for the construction of abundant and stable Ti<sup>3+</sup>-doped photocatalyst.

#### Author contributions

The manuscript was written through contributions of all authors. All authors have given approval to the final version of the manuscript.

#### Acknowledgment

We thank the Program for Harbin Youth Fund (RC2013XK017003 and RC2014QN017004), Youth Fund of Heilongjiang Province (QC2014C006), China Postdoctoral Science Foundation funded project (No 2016T90319), Natural Science Foundation of Heilongjiang Province (B201603) and Heihe University (KJY201702) for the financial support of this research.

#### Appendix A. Supplementary data

Supplementary data associated with this article can be found, in the online version, at <http://dx.doi.org/10.1016/j.apcatb.2017.07.014>.

#### References

- [1] Z. Wang, C. Yang, T. Lin, H. Yin, P. Chen, D. Wan, F. Xu, F. Huang, J. Lin, X. Xie, M. Jiang, Energy Environ. Sci. 6 (2013) 3007–3014.
- [2] C. Mao, F. Zuo, Y. Hou, X. Bu, P. Feng, Angew. Chem. 126 (2014) 10653–10657.
- [3] L. Kai, S. Gao, Q. Wang, H. Xu, Z. Wang, B. Huang, Y. Dai, J. Lu, ACS Appl. Mater. Interfaces 7 (2015) 9023–9030.
- [4] F. Zuo, K. Bozhilov, R.J. Dillon, L. Wang, P. Smith, X. Zhao, C. Bardeen, P. Feng, Angew. Chem. 124 (2014) 6327–6330.
- [5] C. Zhou, Y. Zhao, L. Shang, Y. Cao, L. Wu, C. Tung, T. Zhang, Chem. Commun. 50 (2014) 9554–9556.
- [6] R. Asahi, T. Morikawa, T. Ohwaki, K. Aoki, Y. Taga, Science 293 (2001) 269–271.
- [7] I. Justicia, P. Ordejón, G. Canto, J. Mozos, J. Fraxedas, G. Battiston, R. Gerbasi, A. Figueiras, Adv. Mater. 14 (2004) 1399–1402.
- [8] T.L. Thompson, J.T. Yates, Chem. Rev. 106 (2006) 4428–4453.
- [9] N. Feng, F. Liu, M. Huang, A. Zheng, Q. Wang, T. Chen, G. Cao, J. Xu, J. Fan, F. Deng, Sci. Rep. 6 (2016) 1–9.
- [10] J. Su, X. Zou, Y. Zou, G. Li, P. Wang, J. Chen, Inorg. Chem. 52 (2013) 5924–5930.
- [11] S. Hoang, S.P. Berglund, N.T. Hahn, A.J. Bard, C.B. Mullins, J. Am. Chem. Soc. 134 (2012) 3659–3662.
- [12] F. Zuo, L. Wang, T. Wu, Z. Zhang, D. Borchardt, P. Feng, J. Am. Chem. Soc. 132 (2010) 11856–11857.

[13] M. Liu, X. Qiu, M. Miyauchi, K. Hashimoto, *Chem. Mater.* 23 (2011) 5282–5286.

[14] B. Bharti, S. Kumar, H. Lee, R. Kumar, *Sci. Rep.* 6 (2016) 32355.

[15] X. Chen, L. Liu, P.Y. Yu, S.S. Mao, *Science* 331 (2011) 746–750.

[16] H. Liu, H.T. Ma, X.Z. Li, M. Wu, X.H. Bao, *Chemosphere* 50 (2003) 39–46.

[17] I. Nakamura, N. Negishi, S. Kutsuna, T. Ihara, S. Sugihara, K. Takeuchi, *J. Mol. Catal. A: Chem.* 161 (2000) 205–212.

[18] Z.K. Zhang, M.L. Bai, D.Z. Guo, S.M. Hou, G.M. Zhang, *Chem. Commun.* 47 (2011) 8439–8441.

[19] T. Ihara, M. Miyoshi, *J. Mater. Sci.* 36 (2001) 4201–4207.

[20] M. Xing, J. Zhang, F. Chen, B. Tian, *Chem. Commun.* 47 (2011) 4947–4949.

[21] C. Yang, Z. Wang, T. Lin, H. Yin, X. Lu, D. Wang, T. Xu, C. Zheng, J. Lin, F. Huang, X. Xie, M. Jiang, *J. Am. Chem. Soc.* 135 (2013) 17831–17838.

[22] F.N. Sayed, O.D. Jayakumar, R.M. Kadam, S.R. Bharadwaj, L. Kienle, U. Schürmann, S. Kaps, R. Adelung, J.P. Mittal, A.K. Tyagi, *J. Phys. Chem. C* 116 (2012) 12462–12467.

[23] Q. Kang, J. Cao, Y. Zhang, L. Liu, H. Xu, J. Ye, *J. Mater. Chem. A* 1 (2013) 5766–5774.

[24] X. Zou, G. Li, K. Wang, L. Li, J. Su, J. Chen, *Chem. Commun.* 46 (2010) 2112–2114.

[25] J. Su, X. Zou, G. Li, L. Li, J. Zhao, J. Chen, *Chem. Commun.* 48 (2012) 9032.

[26] L.R. Grabstanowicz, S. Gao, T. Li, R.M. Rickard, T. Rajh, D.J. Liu, T. Xu, *Inorg. Chem.* 52 (2013) 3884–3890.

[27] X. Liu, S. Gao, H. Xu, Z. Lou, W. Wang, B. Huang, Y. Dai, *Nanoscale* 5 (2013) 1870–1875.

[28] Z. Pei, L. Ding, H. Lin, S. Weng, Z. Zheng, Y. Hou, P. Liu, *J. Mater. Chem. A* 1 (2013) 10099–10102.

[29] W. Liu, P. Gao, D. Bao, G. Zhang, Y. Chen, G. Chen, Y. Wang, L. Wang, S. Yang, G. Li, Y. Sun, *RSC Adv.* 3 (2013) 6531–6537.

[30] X. Shao, W. Lu, R. Zhang, F. Pan, *Sci. Rep.* 3 (2013) 3018.

[31] E.M. Rockafellow, X. Fang, B.G. Trewyn, K. Schmidt, W.S. Jenks, *Chem. Mater.* 21 (2009) 1187–1197.

[32] A. Choukourov, A. Grinevich, O. Polonskyi, J. Hanus, J. Kousal, D. Slavinska, H. Biederman, *J. Phys. Chem. B* 113 (2009) 2984–2989.

[33] F. Wang, Y. Jiang, D.J. Lawes, G.E. Ball, C. Zhou, Z. Liu, R. Amal, *ACS Catal.* 5 (2015) 3924–3931.

[34] C. Mao, F. Zuo, Y. Hou, X. Bu, P. Feng, C. Mao, F. Zuo, Y. Hou, X. Bu, P. Feng, *Angew. Chem. Int. Ed.* 53 (2014) 10485–10489.

[35] S. Shanmugam, A. Gabashvili, D. Jacob, J. Yu, A. Gedanken, *Chem. Mater.* 18 (2006) 2275–2282.

[36] Y. Li, Z. Wang, T. Xia, H. Ju, K. Zhang, R. Long, Q. Xu, *Adv. Mater.* 28 (2016) 6959–6965.

[37] Q. Gu, J. Long, H. Zhuang, *Phys. Chem. Chem. Phys.* 16 (2014) 12521–12534.

[38] A. Naldonia, M. D'Arienzo, M. Altomare, M. Marellia, R.S.F. Morazzonib, E. Sellia, *Appl. Catal. B-Environ.* 130–131 (2013) 239–248.

[39] F. Wang, Y. Jiang, D.J. Lawes, G.E. Ball, C. Zhou, Z. Liu, R. Amal, *ACS Catal.* 5 (2015) 3924–3931.

[40] S. Saha, B. Martin, B. Leonardi, D. Li, *J. Mater. Chem. A* 4 (2016) 9253–9265.

[41] B.K. Vijayan, N.M. Dimitrijevic, D. Finkelstein-Shapiro, J. Wu, K.A. Gray, *ACS Catal.* 2 (2012) 223–229.

[42] Y. Kusumawati, A. Martoprawiro, T. Pauporte, *J. Phys. Chem. C* 118 (2014) 9974–9981.

[43] R. Wang, Q. Wu, Y. Lu, H. Liu, Y. Xia, J. Liu, D. Yang, Z. Huo, X. Yao, *ACS Appl. Mater. Interfaces* 6 (2014) 2118–2124.

[44] H. Yu, R. Shi, Y. Zhao, T. Bian, Y. Zhao, C. Zhou, G.I.N. Waterhouse, L. Wu, C. Tung, T. Zhang, *Adv. Mater.* 29 (2017) 1605148.

[45] P. Pyykkö, M. Patzschke, J. Suurpere, *Chem. Phys. Lett.* 381 (2003) 45–52.

[46] E. Thiagarajan, P. Saravanan, S. Shiyamala, P. Saranya, G.N. Nagendra, S. Renganathan, *J. Saudi Chem. Soc.* 5 (2013) 1–4.

[47] Y. Li, Z. Wang, T. Xia, H. Ju, K. Zhang, R. Long, Q. Xu, C. Wang, L. Song, J. Zhu, J. Jiang, Y. Xiong, *Adv. Mater.* 32 (2016) 6959–6965.

[48] J. Huang, Q. Shang, Y. Huang, F. Tang, Q. Zhang, Q. Liu, S. Jiang, F. Hu, W. Liu, Y. Luo, T. Yao, Y. Jiang, Z. Pan, Z. Sun, S. Wei, *Angew. Chem. Int. Ed.* 55 (2016) 2177–2181.

[49] Y. Hou, Z. Wen, S. Cui, X. Guo, J. Chen, *Adv. Mater.* 25 (2013) 6291–6297.

[50] Y. Hou, F. Zuo, A. Dagg, P. Feng, *Nano Lett.* 12 (2012) 6464–6473.

[51] J. Chen, D. Zhao, Z. Diao, M. Wang, S. Shen, *Sci. Bull.* 61 (2016) 292–301.

[52] F. Xiao, S. Hung, H.B. Tao, J. Miao, H.B. Yang, B. Liu, *Nanoscale* 6 (2014) 14950–14961.

[53] X. Yu, J. Zhang, Z. Zhao, W. Guo, J. Qiu, X. Mou, A. Li, J.P. Claverie, H. Liu, *Nano Energy* 16 (2015) 207–217.

[54] H. Yu, R. Shi, Y. Zhao, G.I.N. Waterhouse, L. Wu, C. Tung, T. Zhang, *Adv. Mater.* 28 (2016) 9454–9477.